Supporting Information

Nitrogen-induced interfacial electronic structure of NiS$_2$/CoS$_2$ with optimized water and hydrogen binding abilities for efficient alkaline hydrogen evolution electrocatalysis

Bocheng Qiu,* Yuefeng Zhang, Xuyun Guo, Yingxin Ma, Mengmeng Du, Jun Fan, Ye Zhu, Zhiyuan Zeng,* and Yang Chai*

Experimental Section/Methods

Chemicals. High purity (analytical reagent) chemcials, including $CoCl_2 \cdot 6H_2O$, $NiCl_2 \cdot 6H_2O$, $Na_2S_2O_3 \cdot 5H_2O$, $CuCl_2 \cdot 2H_2O$, NaOH, ascorbic acid, thioacetamide, and sulfur powder, were purchased from Aladdin. Polyvinyl pyrrolidone (PVP, K30) and Platinum on carbon (Pt/C, 20 wt. %) were purchased from Alfa Aesar Chemical Co., Ltd. Carbon paper was purchased from CeTech Co., Ltd. The water used all the experiments were de-ionized.

Preparation of Cu₂O nanocubes. The Cu_2O nanocubes were synthesized by the previously reported method.[1] Typically, 170 mg $CuCl_2 \cdot 2H_2O$ was dissolved in 100 mL water and heated to 55 °C. Then, 10 mL 2 M NaOH was slowly dropped into the above solution to form a brown suspension. After 30 min stirring, 10 mL 0.6 M ascorbic acid was dropwise introduced into the suspension. After aging for 3 h, the Cu_2O precipitate was collected by centrifugation, followed by washing with water two times and ethanol once, and finally dried in a vacuum at 40 °C overnight.

Preparation of Ni(OH)₂/Co(OH)₂ nanocages. 20 mg Cu_2O powder was dispersed into the mixed solvent comprised of 20 mL deionized (DI) water and 20 mL ethanol with the assistance of ultrasound treatment. Afterwards, 3.4 mg $CoCl_2 \cdot 6H_2O$ and 1.7 mg $NiCl_2 \cdot 6H_2O$ (the ratio of Ni/Co is 1:2) were added into the above suspension under magnetic stirring. After stirring for 30 min, 330 mg polyvinyl pyrrolidone (PVP, K30) was dissolved into the solution. After stirring for another 30min, 50 mL 1 M $Na_2S_2O_3$ solution was drop-by-drop introduced into the suspension. Once the color of the solution completely changed from brick-red to transparent green, the resulting precipitate was centrifuged and washed by DI water and ethanol, and finally vacuum-dried at 40 °C. Besides, the $Ni(OH)_2/Co(OH)_2$ nanocages with other Ni/Co molar ratios (1:1 and 1:3) were also prepared. Note that the total addition masses for $CoCl_2 \cdot 6H_2O$ and $NiCl_2 \cdot 6H_2O$ is kept at 5.1 mg. As for the bare $Co(OH)_2$ or $Ni(OH)_2$ nanocages, the preparation procedure is similar to that of $Ni(OH)_2/Co(OH)_2$ nanocages, except that 3.4 mg $CoCl_2 \cdot 6H_2O$ and 1.7 mg $NiCl_2 \cdot 6H_2O$ were replaced by 5.1 mg $CoCl_2 \cdot 6H_2O$ or 5.1 mg $NiCl_2 \cdot 6H_2O$, respectively.

Preparation of N-NiS₂/CoS₂ nanocages. Typically, the N-NiS₂/CoS₂ powders with different Ni/Co ratios were obtained by annealing their corresponding $Ni(OH)_2/Co(OH)_2$ nanocages (50 mg) and thiourea powder (500 mg) at 350 °C for 2 h with a heating rate of 10 °C min⁻¹ under a flow of Ar atmosphere. Note that thiourea powder was located at the upstream side of the furnace and the $Ni(OH)_2/Co(OH)_2$ powder was placed at the downstream side.

Preparation of NiS₂/CoS₂ nanocages. The synthesis procedure of NiS₂/CoS₂ nanocages was similar to that of N-NiS₂/CoS₂ nanocages except using sulfur powder instead of thiourea powder.

Preparation of NiS₂ nanocages. The synthetic method of NiS₂ nanocages was similar

to that of NiS_2/CoS_2, except that $Ni(OH)_2/Co(OH)_2$ was replaced by $Ni(OH)_2$.

Preparation of CoS$_2$ nanocages. The synthetic method of CoS_2 was similar to that of NiS_2/CoS_2, except that $Ni(OH)_2/Co(OH)_2$ was replaced by $Co(OH)_2$.

Materials Characterizations. Field-emission scanning electron microscope (FESEM) carried out on TESCAN MIRA3 was employed to observe the surface morphology of the samples. Transmission electron microscope (TEM), high resolution transmission electron microscope (HRTEM), and energy-dispersive X-ray spectroscopy (EDX) attached to the HRTEM were recorded on JEOL 2100F. HAADF-STEM image and elemental mapping were collected using a TEM (JEOL, JEM-2100F) equipped with EDX spectroscopy. XRD patterns of all the samples were recorded on a RigakuD/MAX 2550 diffract meter (Cu K radiation, $\lambda = 1.5406$ Å) operated at 40 kV and 100 mA and collected in the range from 10° to 80° (2θ). Surface area measurements of the samples were conducted on an ASAP2020 instrument at 77 K. The chemical states of the samples were analyzed by X-ray photoelectron spectroscopy (XPS, Perkin-Elmer PHI 5000C ESCA) using Al Kα radiation operated at 250 W with C 1s (284.6 eV) as calibration reference.

Electrochemical Measurements. Catalysts (5 mg) were dispersed in 760 μL of ethanol, 200 μL of DI water and 40 μL of 5 wt% Nafion solution to form a homogeneous ink with the assistance of ultrasound treatment. For the preparation of working electrodes, 20 μL of catalyst inks was homogeneously dispersed onto the carbon fiber paper (0.25 cm^2) and then dried at room temperature. The mass loading of catalysts was calculated to 0.4 mg cm^{-2}. The Pt/C electrode was prepared with the same catalysts loading of 0.4 mg cm^{-2} (Note that the Pt loading amount was calculated to be 80 μg cm^{-2}). Graphite and Hg/HgO electrode were used as the counter electrode and reference electrode, respectively. Potentials were referenced to a reversible hydrogen electrode (RHE): $E_{RHE} = E_{Hg/HgO} + 0.098 + 0.059 \times pH$. The overpotential ($\eta$) was calculated according to the following formula: $\eta = E_{RHE}$. Linear sweep voltammetry (LSV) was recorded in a H_2-saturated 1.0 M KOH at a scan rate of 5 mV s^{-1}. All the polarization curves presented were corrected for IR loss (The introduction of IR corrected polarization curves makes up for the electrode potential loss at medium to high current region caused by the solution resistance). The compensated potential was corrected by $E_{compensated} = E_{measured} - i \times R_S$, where R_S was determined by the electrochemical workstation. The stability tests were carried out by cyclic voltammetry (CV) sweeps from -0.2 to 0.1V (*vs* RHE) at the scan rate of 50 mV s^{-1} for 2000 cycles and chronopotentiometry at a constant current density of 10 and 50 mA cm^{-2}. The electrochemical impendence spectroscopy (EIS) measurements were measured at an overpotential of 100 mV in the frequency range of 0.1 to 100k Hz with an amplitude of 5 mV. The electrochemical active surface area (ECSA) was calculated from the CV curves measured in a potential range from 0.89 to 0.99 V (E *vs*. RHE) in terms of the following equation: $C_{dl} = (j_a - j_c)/(2 \bullet v) = \Delta j/(2 \bullet v)$, where C_{dl},

j_a, j_c and ν are the double-layer capacitance (F cm^{-2}), the anodic current density (mA cm^{-2}), the cathodic current density (mA cm^{-2}), and scan rate (mV s^{-1}), respectively. Note that j_a and j_c were recorded at 0.94 V (*Vs*. RHE) and the slope of the Δj *vs* scan rate curve is just twice of the value of C_{dl}. The roughness factors (RF) of different samples from their C_{dl} values by using the equation: RF = C_{dl}/C_s, where C_s is the double layer capacitance of an ideally flat electrode, which is usually taken as 40 µF cm^{-2} in an alkaline electrolyte according to the typical references.[2]

Density Functional Theory Calculations. All the calculations were carried out by employing periodic density functional theory methods as implemented in the Vienna ab-initio simulation package(VASP)[3, 4]. The interaction between atomic cores and valence electrons was represented by the projector augmented wave (PAW). The generalized gradient approximation (GGA) with the Perdew-Burke-Ernzerhof (PBE) functional[5] was used for the exchange-correlation energies. The effective U parameter was set as 3.5 eV for the 3d states of Co and Ni.[6] The cut off energy was set at 420 eV. The geometry convergence criterion for the maximum force on each atom is set to be less than 0.02 eV/Å. In K-sampling, a Monkhorst mesh of 2×2×1 was considered for structural optimization. The vacuum layer thickness is set to be 15 Å to avoid interactions among interlayers. The lateral heterojunction model was constructed by using CoS$_2$ (200) plane and NiS$_2$ (200) plane. The bottom two layers of heterojunction are fixed at bulk truncated positions during optimisation while the remaining atoms relaxed. The N-NiS$_2$/CoS$_2$ model was constructed by replacing a sulfur atom near the interface with a N atom. The climbing image nudged elastic band (CI-NEB) method[7] was used to calculate the reaction energy barriers, and the relaxed transition state was verified by vibration frequency analysis. In terms of hydrogen evolution reaction (HER), the free energy change for H adsorption on heterojunction models were defined as:

$$\Delta G_H = E_{total} - E_{sur} - \frac{1}{2}E_{H2} + \Delta E_{ZPE} - T\Delta S$$

Where E_{total}, E_{sur}, E_{H2} are the calculated energies of the adsorption state, a clean surface and a molecule hydrogen, respectively. T is the temperature, ΔE_{ZPE} and ΔS are the correction of the zero point energy and entropy, respectively.
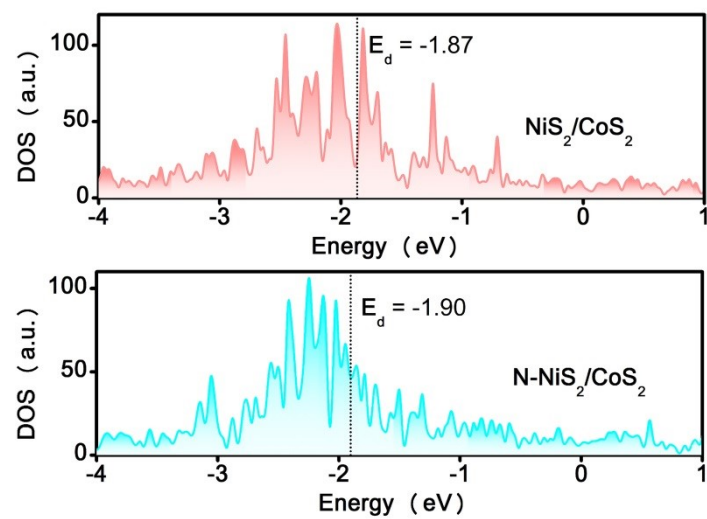
Fig. S1 The projected d-band density of states (DOS) of NiS_2/CoS_2 and $N-NiS_2/CoS_2$.
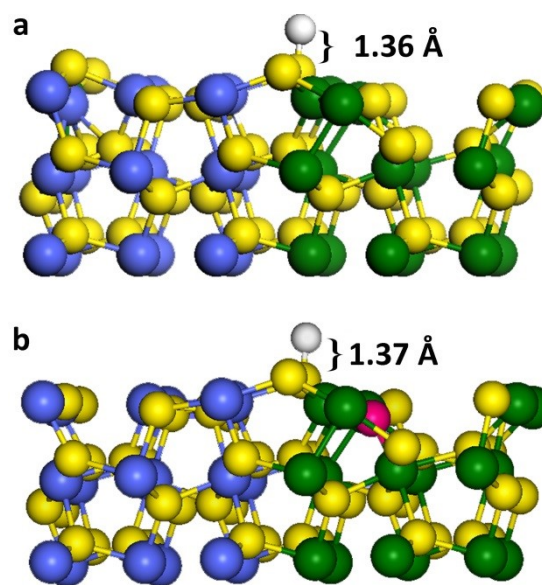
a } 1.36 Å

b } 1.37 Å

Fig. S2 The variations of the S-H$_{ads}$ bond length (a) before and (b) after N doping.
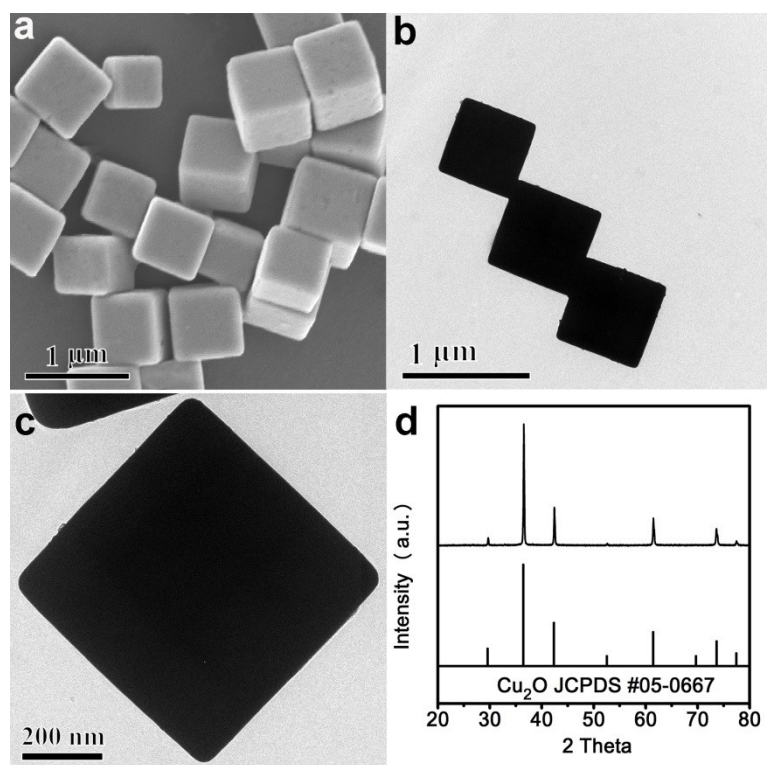
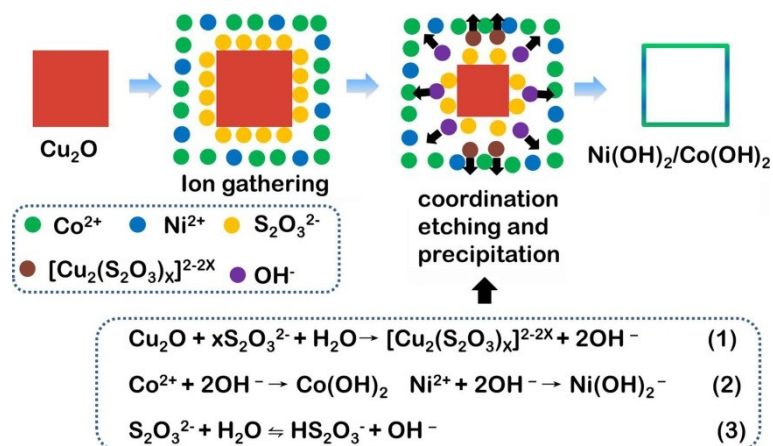**Fig. S3** (a) SEM image, (b,d) TEM images, and (d) XRD pattern of Cu_2O nanocubes.

Fig. S4 Schematic illustration of the preparation of $Ni(OH)_2/Co(OH)_2$ nanocages.

Coordination etching of Cu_2O templates is based on the stronger interaction between Cu^+ and $S_2O_3^{2-}$ relative to the interaction of Cu^+-O^{2-} within the Cu_2O templates (Equation 1). The OH^- ions generated from Cu_2O etching can facilitate the precipitation of Co^{2+} and Ni^{2+} (Equation 2), and meanwhile the exhaustion of OH^- for the production of $Ni(OH)_2/Co(OH)_2$ offers a driving force for the hydrolysis of $S_2O_3^{2-}$ ions (Equation 3). Note that the PVP molecule as a surfactant participates in the coordination etching and precipitation reaction.
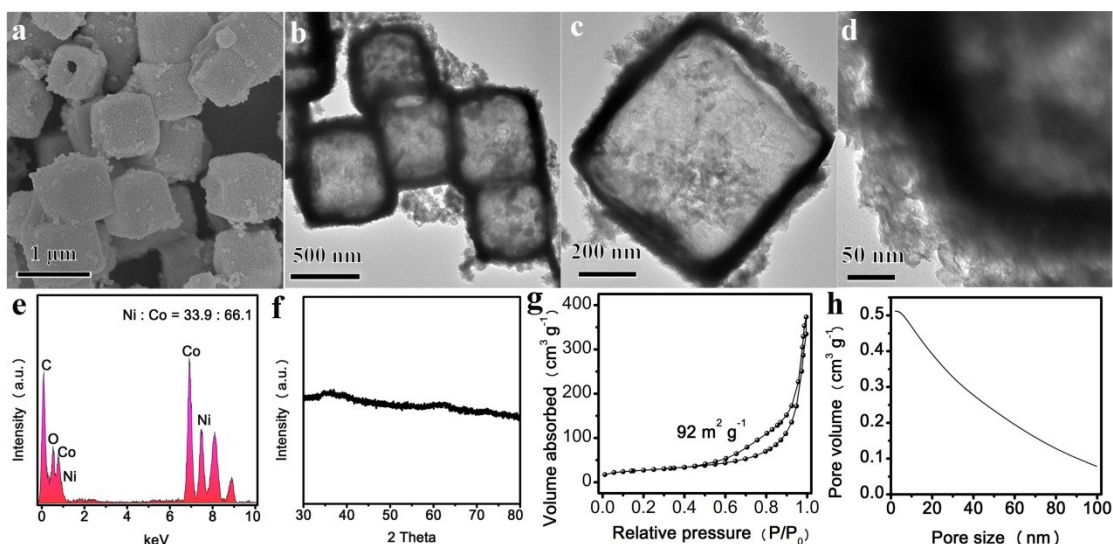
Fig. S5 (a) SEM, (b-d) TEM images, (e) EDX spectrum, (f) XRD pattern, (g) N_2 adsorption-desorption curve and (h) its corresponding pore size distribution of $Ni(OH)_2/Co(OH)_2$ nanocages.

SEM (Fig. S5a) and TEM (Fig. S5b-d) observations demonstrate that the obtained $Ni(OH)_2/Co(OH)_2$ products enable a high-quality cavity structure with an exterior diameter of 750 nm, and meanwhile inherit the geometrics and dimensions of the Cu_2O nanocubes templates well. The corresponding EDX spectrum (Fig. S5e) reveals that the ratio of Ni/Co is close to the addition ratio (1:2). Besides, the XRD pattern (Fig. S5f) indicates the complete removal of Cu_2O templates and the formation of an amorphous structure of the $Ni(OH)_2/Co(OH)_2$ product. The N_2 adsorption-desorption measurements (Figure S5g-h) exhibit a high surface area of 92 m^2 g^{-1} and the presence of macro/mesoporous structure.

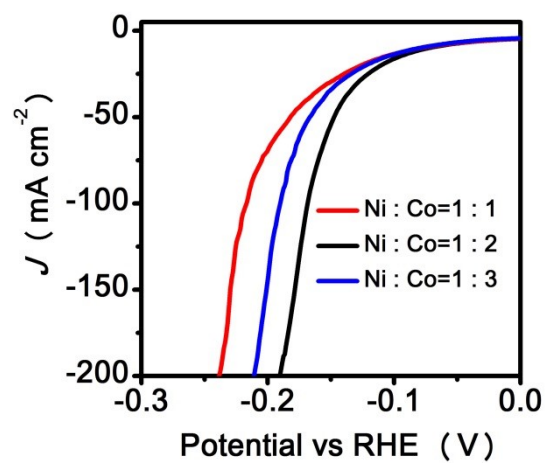**Fig. S6** The LSV curves of N-NiS$_2$/CoS$_2$ interfaces with different NiS$_2$/CoS$_2$ ratios.
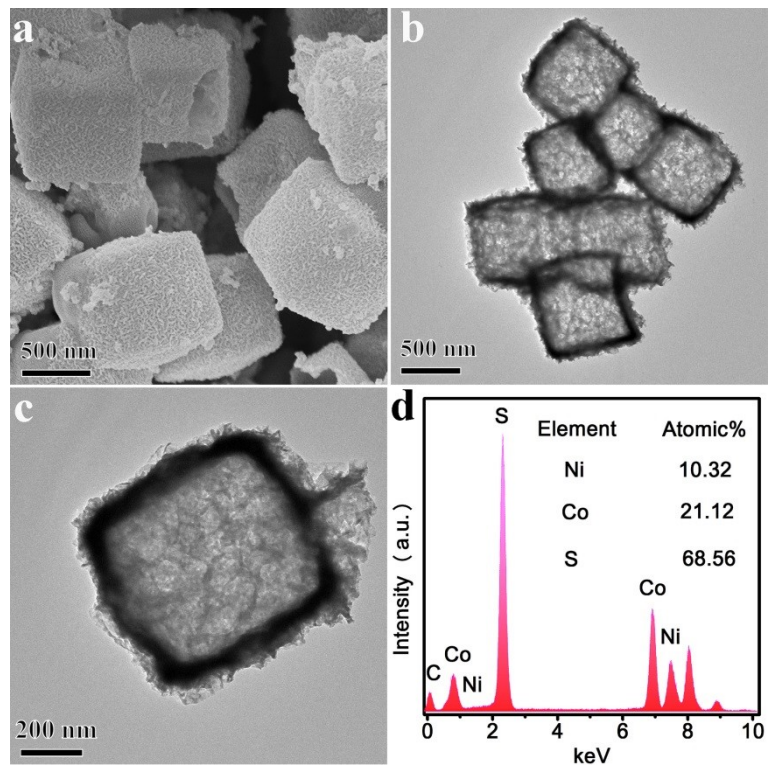
Fig. S7 (a) SEM image, (b,c) TEM images, and (d) their corresponding EDX spectrum of NiS$_2$/CoS$_2$.

The NiS$_2$/CoS$_2$ nanocages were synthesized by the thermal treatment of sulfur powder and the Ni(OH)$_2$/Co(OH)$_2$ at Ar atmosphere. The as-obtained NiS$_2$/CoS$_2$ product well inherited the hollow structure of Ni(OH)$_2$/Co(OH)$_2$ (Fig. S7a-c). The EDX spectrum (Fig. S7d) and XRD pattern (Fig. 3h) consistently revealed the NiS$_2$/CoS$_2$ products existed in the form of NiS$_2$/CoS$_2$ heterostructure with the NiS$_2$/CoS$_2$ molar ratio of 1:2.
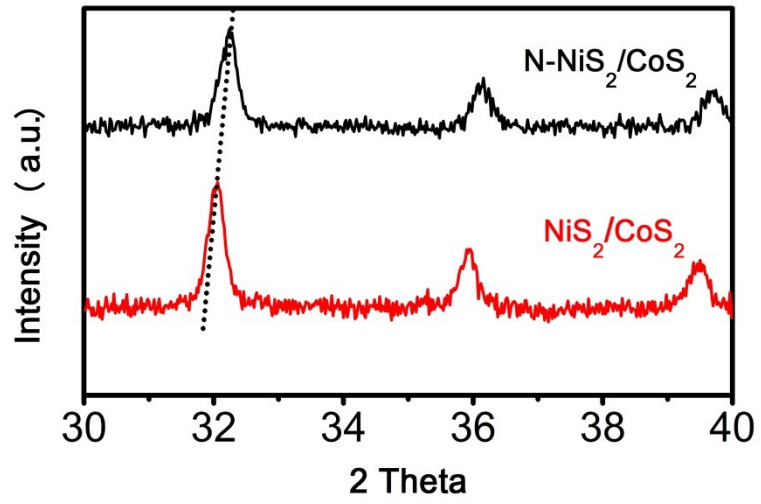
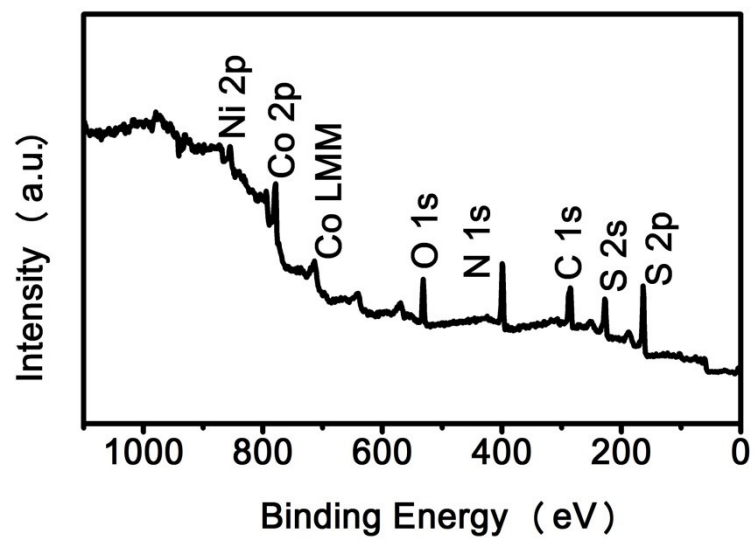**Fig. S8** Partially enlarged area of XRD patterns in Fig. 3h.

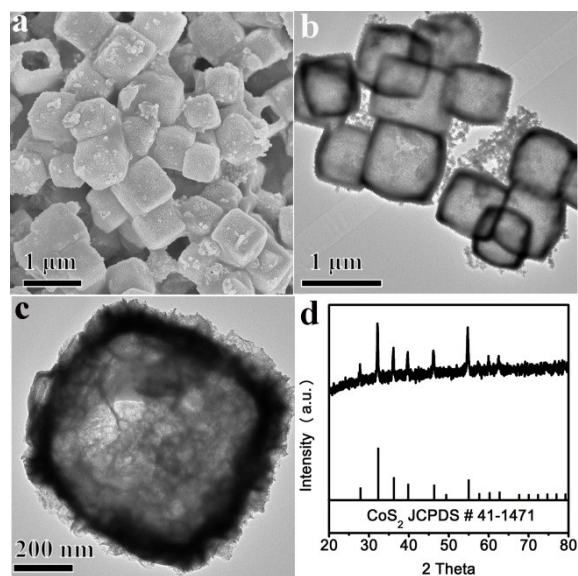**Fig. S9**. XPS survey spectrum of N-NiS$_2$/CoS$_2$.

Fig. S10 (a) SEM image, (b,c) TEM images, and (d) their corresponding XRD patterns of CoS$_2$.

The obtained CoS$_2$ samples show an average side length of 750 nm and well-defined hollow structure, as revealed by the SEM (Fig. S10a) and TEM (Fig. S10b,c) images. The XRD pattern (Fig. S10d) demonstrates that the typical peaks are indexed into the cubic CoS$_2$ structure (JCPDS 41-1471).
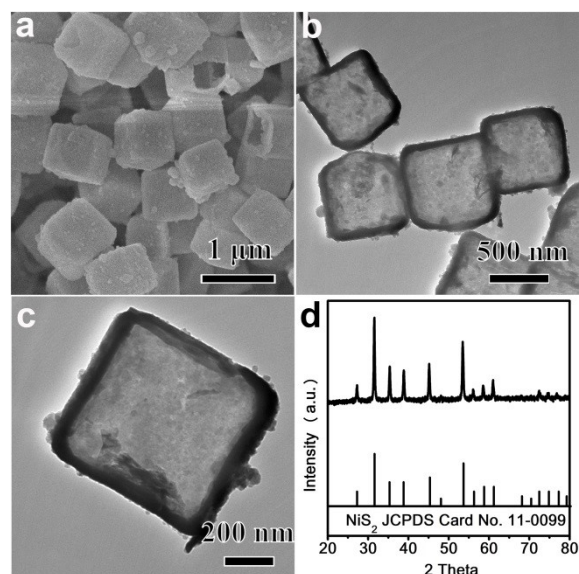
Fig. S11. (a) SEM image, (b,c) TEM images, and (d) their corresponding XRD patterns of NiS$_2$.

The as-prepared NiS$_2$ sample inherits the dimension and geometry structure of Cu$_2$O templates, and exhibits a cavity structure with an average side length of 750 nm, as indicated by SEM (Fig. S11a) and TEM (Fig. S11b,c) observations. XRD patterns of the obtained product clearly present the presence of the cubic NiS$_2$ structure (Fig. S11d).
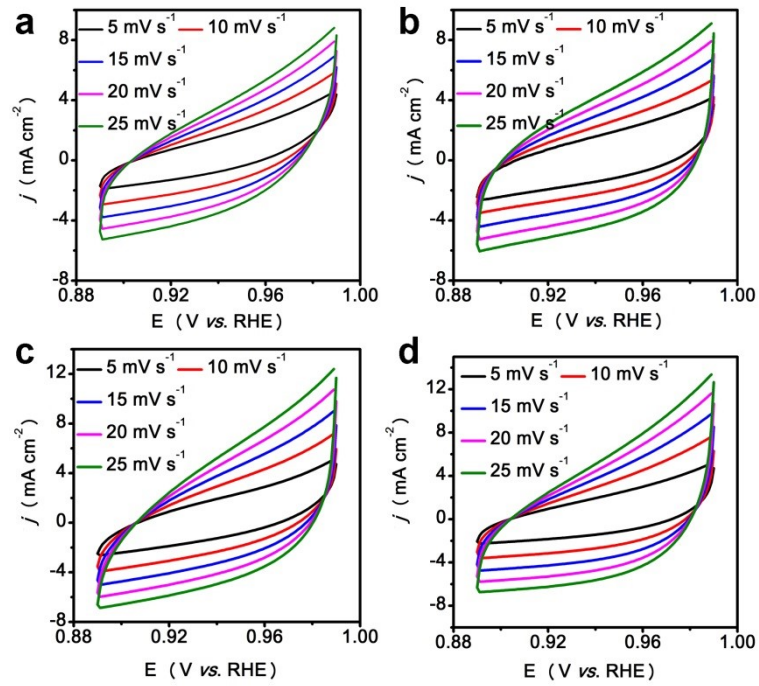
Fig. S12. Cyclic voltammetry curves for (a) NiS_2, (b) CoS_2, (c) NiS_2/CoS_2, and (d) N-NiS_2/CoS_2 in the non-Faradaic capacitive range at the scanning rate of 5, 10, 15, 20, and 25 mV s^{-1}.
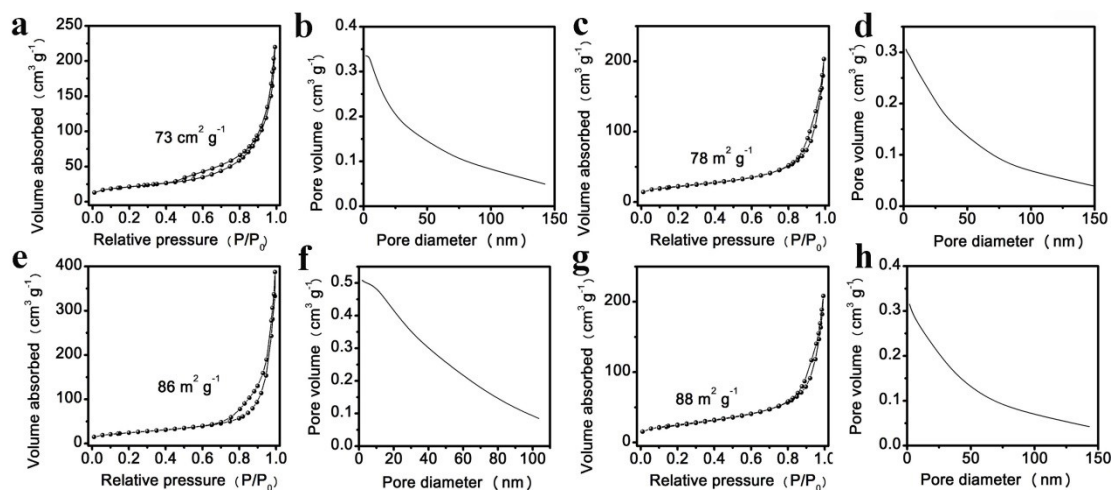
Fig. S13 N$_2$ adsorption-desorption curves and their corresponding pore diameter distribution curves: (a,b) NiS$_2$, (c,d) CoS$_2$, (e,f) NiS$_2$/CoS$_2$, and (g,h) N-NiS$_2$/CoS$_2$

N$_2$ adsorption-desorption curves display that N-NiS$_2$/CoS$_2$ enables a higher surface area of 88 m^2 g^{-1} as compared to that of NiS$_2$, CoS$_2$, and NiS$_2$/CoS$_2$, suggesting the most catalytic sites on N-NiS$_2$/CoS$_2$, which accords with the result of ECSAs.
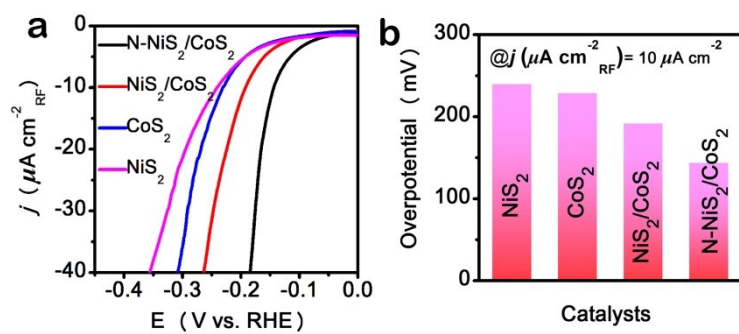
Fig. S14 Normalized specific activities by RFs of different catalysts: (a) LSV curves and (b) overpotentials at the current density of 10 μA cm^{-2}.

Fig. S15 (a) SEM and (b) TEM images of the recovered N-NiS$_2$/CoS$_2$ sample after HER. (c) A comparison of XRD patterns of N-NiS$_2$/CoS$_2$ before and after HER.

Fig. S16 High resolution XPS spectra of (a) N 1s, (b) Co 2p, (c) Ni 2p, and (d) S 2p for N-NiS$_2$/CoS$_2$ before and after HER.

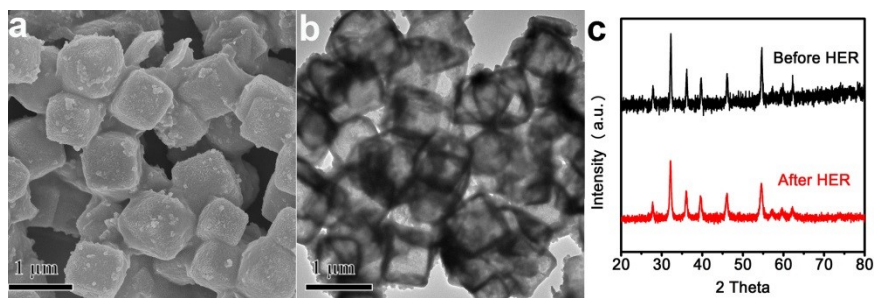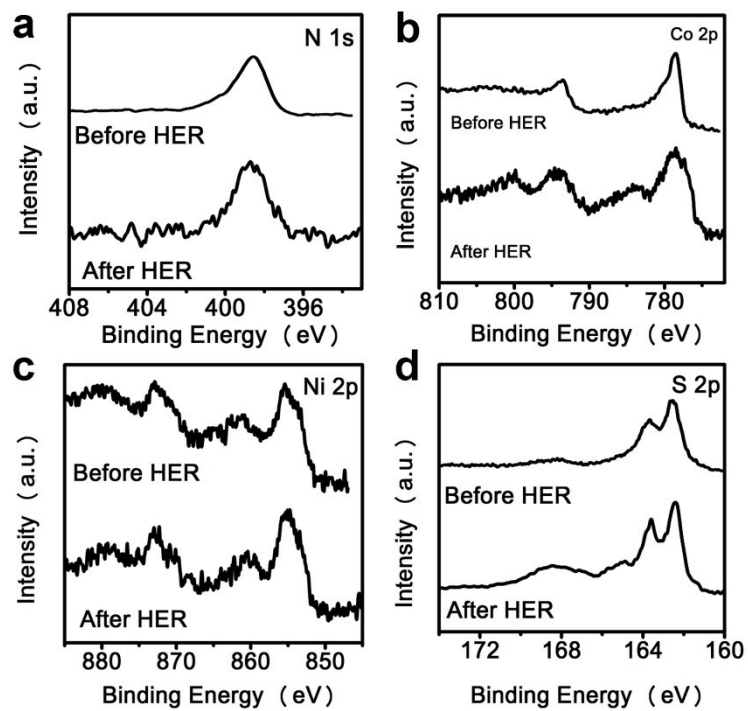**Fig. S17** (a) Chronopotentiometric curves at a constant current density of 50 mA cm^{-2}. (b) SEM images of the recovered N-NiS$_2$/CoS$_2$ sample after HER. (c) A comparison of XRD patterns of N-NiS$_2$/CoS$_2$ before and after HER.

Table S1. Element composition ratio of N-NiS$_2$/CoS$_2$ by using XPS analysis.

Catalysts	N (atomic%)	Ni (atomic%)	Co (atomic%)	S (atomic%)
N-NiS$_2$/CoS$_2$	1.11	10.73	22.82	65.34

Table S2. The summary of recently reported metal sulfides-based HER catalysts.

Catalysts	η_{10} (mV)	Tafel slope (mV dec^{-1})	Electrolyte	Ref.
FeS$_2$/CoS$_2$	78	42	1.0 M KOH	[8]
Co-MoS$_2$/Ni$_3$S$_2$	89	62	1.0 M KOH	[9]
NiS$_2$/MoS$_2$	204	65	1.0 M KOH	[10]
CoS$_2$/MoS$_2$	82	59	1.0 M KOH	[11]
NiS@CoS	30	97	1.0 M KOH	[12]
NiS$_2$/CoS$_2$/MoS$_2$	112	59	1.0 M KOH	[13]
O-CoS$_2$/MoS$_2$	97	70	1.0 M KOH	[14]
MoS$_2$/NiS	92	113	1.0 M KOH	[15]
MoS$_2$/Ni$_3$S$_2$	98	61	1.0 M KOH	[16]
Co$_9$S$_8$/Ni$_3$S$_2$	128	98	1.0 M KOH	[17]
MoS$_2$/NiS$_2$	62	50	1.0 M KOH	[18]
N-NiS$_2$/CoS$_2$	73	65	1.0 M KOH	This work

Table S3. The calculated RF values of different samples.

Catalyst	NiS$_2$	CoS$_2$	NiS$_2$/CoS$_2$	N-NiS$_2$/CoS$_2$
RF	2925	3525	4350	4550

Table S4. The fitted results of the EIS plots in Fig. 5e.

Catalyst	NiS$_2$	CoS$_2$	NiS$_2$/CoS$_2$	N-NiS$_2$/CoS$_2$
R_s (Ω)	0.8	0.8	0.8	0.8
R_{CT} (Ω)	33.0	17.3	13.0	7.1
R_{Por} (Ω)	2.3	2.7	1.5	0.9

Reference

[1]   B. Qiu, L. Cai, Y. Wang, X. Guo, S. Ma, Y. Zhu, Y. H. Tsang, Z. Zheng, R. Zheng, Y. Chai, *Small* **2019**, 15, 1904507.

[2]   C. C. McCrory, S. Jung, J. C. Peters, T. F. Jaramillo, *J. Am. Chem. Soc.* **2013**, 135, 16977.

[3]   G. Kresse, J. Furthmüller, *Comput. Mater. Sci.* **1996**, 6, 15.

[4]   G. Kresse, J. Furthmüller, *Phys. Rev. B* **1996**, 54, 11169.

[5]   J. P. Perdew, K. Burke, M. Ernzerhof, *Phy. Rev. Lett.* **1996**, 77, 3865.

[6]   J. Yin, Y. Li, F. Lv, M. Lu, K. Sun, W. Wang, L. Wang, F. Cheng, Y. Li, P. Xi, *Adv. Mater.* **2017**, 29, 1704681.

[7]   G. Henkelman, B. P. Uberuaga, H. Jónsson, *J. Chem. Phys.* **2000**, 113, 9901.

[8]   Y. Li, J. Yin, L. An, M. Lu, K. Sun, Y. Q. Zhao, D. Gao, F. Cheng, P. Xi, *Small* **2018**, 14, 1801070.

[9]   L. Zhang, Y. Zheng, J. Wang, Y. Geng, B. Zhang, J. He, J. Xue, T. Frauenheim, M. Li, *Small* **2021**, 17, 2006730.

[10]   P. Kuang, T. Tong, K. Fan, J. Yu, *ACS Catal.* **2017**, 7, 6179.

[11]   Y. Li, W. Wang, B. Huang, Z. Mao, R. Wang, B. He, Y. Gong, H. Wang, *J. Energy Chemistry* **2021**, 57, 99.

[12]   Y. Yang, Y. Zhang, Y. Zhou, C. Zhu, Y. Xie, L. Lv, W. Chen, Y. He, Z. Hu, *Int. J. Hydrogen Energy* **2019**, 44, 26753.

[13]   Y. Zhang, M. Shi, C. Wang, Y. Zhu, N. Li, X. Pu, A. Yu, J. Zhai, *Sci. Bull.* **2020**, 65, 359.

[14]   J. Hou, B. Zhang, Z. Li, S. Cao, Y. Sun, Y. Wu, Z. Gao, L. Sun, *ACS Catal.* **2018**, 8, 4612.

[15]   Z. Zhai, C. Li, L. Zhang, H.-C. Wu, N. Tang, W. Wang, J. Gong, *J. Mater. Chem. A* **2018**, 6, 9833.

[16]   Y. Yang, K. Zhang, H. Lin, X. Li, H. C. Chan, L. Yang, Q. Gao, *ACS Catal.* **2017**, 7, 2357.

[17]   F. Du, L. Shi, Y. Zhang, T. Li, J. Wang, G. Wen, A. Alsaedi, T. Hayat, Y. Zhou, Z. Zou, *Appl. Catal. B: Environ.* **2019**, 253, 246.

[18]   J. Lin, P. Wang, H. Wang, C. Li, X. Si, J. Qi, J. Cao, Z. Zhong, W. Fei, J. Feng, *Adv. Sci.* **2019**, 6, 1900246.